Compressible and Recyclable Monolithic g-C$_3$N$_4$/Melamine Sponge: A Facile Ultrasonic-Coating Approach and Enhanced Visible-Light Photocatalytic Activity

Ye Yang [1,2], Qian Zhang [1]*, Ruiyang Zhang [1], Tao Ran [1], Wenchao Wan [1] and Ying Zhou [1,2]*

[1] The Center of New Energy Materials and Technology, School of Materials Science and Engineering, Southwest Petroleum University, Chengdu, China, [2] State Key Laboratory of Oil and Gas Reservoir Geology and Exploitation, Southwest Petroleum University, Chengdu, China

Powdery photocatalysts seriously restrict their practical application due to the difficult recycle and low photocatalytic activity. In this work, a monolithic g-C$_3$N$_4$/melamine sponge (g-C$_3$N$_4$/MS) was successfully fabricated by a cost-effective ultrasonic-coating route, which is easy to achieve the uniform dispersion and firm loading of g-C$_3$N$_4$ on MS skeleton. The monolithic g-C$_3$N$_4$/MS entirely inherits the porous structure of MS and results in a larger specific surface area (SSA) than its powdery counterpart. Benefit from this monolithic structure, g-C$_3$N$_4$/MS gains more exposed active sites, enhanced visible-light absorption and separation of photogenerated carriers, thus achieving noticeable photocatalytic activity on nitric oxide (NO) removal and CO$_2$ reduction. Specifically, NO removal ratio is as high as 78.6% which is 4.5 times higher than that of the powdery g-C$_3$N$_4$, and yield rate of CO and CH$_4$ attains 7.48 and 3.93 μmol g^{-1} h^{-1}. Importantly, the features of low-density, high porosity, good elasticity, and firmness, not only endow g-C$_3$N$_4$/MS with flexibility in various environmental applications, but also make it easy to recycle and stable for long-time application. Our work provides a feasible approach to fabricate novel monolithic photocatalysts with large-scale production and application.

Keywords: g-C$_3$N$_4$/melamine sponge, photocatalysis, NO removal, monolith, visible light

INTRODUCTION

Semiconductor photocatalysis is one of the promising strategies for pollutants abatement (Maggos et al., 2007; Huang et al., 2013, 2016; Zhao et al., 2015) and has attracted intense investigation in the past decades. Up to now, hundreds of semiconductors have been explored and applied in the field of environmental remediation (Liu et al., 2008; Hossain and Mukherjee, 2013; Huang et al., 2015a, 2017a; Zhou et al., 2016). However, only a few of them have been considered as potential candidates for practical application in view of their nontoxic, suitable band gap, band edge energy, good stability and earth-abundant source. g-C$_3$N$_4$ is one of those semiconductors, which possesses graphene-like structure and constituted mainly by carbon and nitrogen. Since g-C$_3$N$_4$ was first reported to photocatalytic water splitting

by Wang et.al (Wang et al., 2009), it quickly becomes a hot material in photocatalysis. Afterwards, $g\text{-}C_3N_4$ has already been applied in various reactions such as CO_2 photoreduction, NO removal, and dye degradation (Yan et al., 2009; Dong et al., 2014a; Sun H. et al., 2017). However, extensive studies revealed that $g\text{-}C_3N_4$ suffers from fast photo-generated carriers recombination, limited visible-light absorption, and low surface area. Various strategies have been carried out to overcome these intrinsic drawbacks of $g\text{-}C_3N_4$, such as elemental doping, composite with other materials and morphology control synthesis, etc. (Liu et al., 2010; Zhao et al., 2012; Hou et al., 2014; Cheng et al., 2015; Han Q. et al., 2015; Li et al., 2017; Yang et al., 2017). Besides above disadvantages, as a potential photocatalyst for practical application, $g\text{-}C_3N_4$ is also hindered by difficult recycle originating from particle heavy loss during its complicated recovery process, inefficient utilization of active sites and light energy resulting from particle aggregation. Comparison with the intrinsic drawbacks of $g\text{-}C_3N_4$, these problems are vital to achieve successful application of photocatalyst on actual environmental issues, but they are rarely studied and generally beyond the aforementioned strategies to overcome.

Recently, monolithic or integrated photocatalysts are found to be a plausible way to solve the practical application problem of photocatalyst (Cheng et al., 2016; Wan et al., 2018). The so-called monolithic photocatalyst usually consists of two parts, one is a macroscopical support with porous three-dimensional (3D) skeleton, and the other is the loaded photocatalyst particles. After integrating powdery catalysts on its support, their recycling becomes easy to achieve by a tweezer (Liu W. J. et al., 2015; Tang et al., 2017). Meanwhile, the 3D porous structure of support gives the powdery catalysts a high dispersion and exposes more active sites by avoiding particles agglomeration. Moreover, this structure also benefits light energy harvest and transportation of liquid or gas pollutants. Until now, graphene aerogels are the most studied monolithic photocatalyst supports because of their inherent large surface area, high porosity and low density. We have fabricated monolithic C_3N_4/graphene oxide aerogel (GOA) in our previous work and found obvious activity enhancement (Wan et al., 2016), which is in line with the results from other monolithic photocatalyst/graphene aerogels (Fan et al., 2015; Cui et al., 2017; Wang et al., 2017). However, the intrinsic brittleness and weak firmness of aerogels make it easy to break into pieces during mechanical deformation, which seriously restrict its potential in practical application. Other firm supports, such as carbon foam and Al_2O_3 ceramic foam with hard 3D framework, are also selected to fabricate monolithic photocatalyst (Dong et al., 2014b; Lin et al., 2016). Nevertheless, it is very difficult to achieve uniform loading by directly mixing photocatalyst with these hard supports. To overcome this problem, special strategies with high cost and energy consumption, like *in-situ* immobilizing approach and laser ablating deposition (Liang et al., 2015; Lin et al., 2016), are used to achieve the good catalyst dispersion. The sophisticated preparation method severely limits the hard supports to be extensively utilized in fabrication of monolithic photocatalyst. Based on the above considerations, the proper support remains an obstacle for the practical application of monolithic photocatalyst. Lately, melamine sponge (MS), a

cheap commercial polymer foam which is widely used as kitchen and construction materials, is successfully used for oil-water separation by integrating with graphene (Liu T. T. et al., 2015; Zhao et al., 2016). The fabricated graphene/MS exhibits low-density, high porosity and high elasticity inherited from MS, which exactly match the support characteristics of the monolithic photocatalyst. Importantly, the good elasticity makes MS more ductile and avoids the drawbacks of brittle and hard materials. Therefore, MS is a potential alternative and selected as the support for monolithic photocatalyst fabrication.

Herein, we prepare a monolithic $g\text{-}C_3N_4$/MS by a facile ultrasonic-coating method at room temperature, which is very easy to achieve mass production. The monolithic structure endows $g\text{-}C_3N_4$/MS with enhanced light harvest and more exposed active sites, ensuring its good photocatalytic activity. Importantly, the as-prepared monolithic photocatalyst exhibits low-density, high porosity, high elasticity and good firmness, which not only make it flexible in various environmental applications including NO removal, and CO_2 photoreduction, but also make it easy to recycle and suitable for practical application. Overall, our results provide a novel strategy to develop monolithic photocatlyst for practical application with large-scale production.

EXPERIMENTAL

Synthesis of g-C$_3$N$_4$

The polymeric $g\text{-}C_3N_4$ was prepared by pyrolysis of urea (Liu et al., 2011). In a typical process, 15 g urea was added into an alumina crucible with a cover and then heated to 550°C in a muffle furnace for 1 h with a heating rate of about 55°C min^{-1}. After cool down to room temperature, the final yellow agglomerates were the pristine $g\text{-}C_3N_4$ and subsequently ground into powder for further use.

Preparation of Monolithic g-C$_3$N$_4$/MS

For the preparation of monolithic $g\text{-}C_3N_4$/MS, 2.5 g $g\text{-}C_3N_4$ powder was dispersed in 500 mL water and sonicated for 1 h to form a $g\text{-}C_3N_4$ suspension. MS was cut into suitable size and washed with deionized water and alcohol in order, then dried at room temperature. Next, the clean MS was immersed into $g\text{-}C_3N_4$ suspension for 30 min, and then squeezed out the excess solution. After that, the sample was transferred into a culture dish and freeze-dried (−70°C pre-freezing) for 48 h to obtain $g\text{-}C_3N_4$/MS. For comparison, powdery $g\text{-}C_3N_4$ without MS was processed through the same procedures and denoted as sonicated $g\text{-}C_3N_4$. To obtain the best photocatalytic activity of monolithic $g\text{-}C_3N_4$/MS, we finely investigated the effect of $g\text{-}C_3N_4$ suspension concentration (3 mg mL^{-1}-40 mg mL^{-1}) and MS thickness (0.5–2.5 cm). The sizes of monolithic $g\text{-}C_3N_4$/MS varied with different experiments and were stated at their first appearance in the text.

Characterization

Powder X-ray diffraction (PXRD) was performed on a PANalytical X'pert diffractometer with a Cu Ka radiation. Transmission electron microscopy (TEM) was performed on

a FEI tecnai G2 F30 microscope operated at 200 kV. The morphology of g-C_3N_4/MS was observed through scanning electron microscopy (SEM) on a ZEISS EVO MA15 microscopy. The Fourier transform infrared (FT-IR) spectra were measured using a Nicolet 6700 spectrometer on samples embedded in KBr pellets. UV-vis diffuse reflectance spectrum (DRS) data were recorded on a Shimadzu UV-2600 spectrophotometer. Photoluminescence spectra were recorded on F-7000 FL spectrofluorometer with an excitation wavelength at 320 nm. X-ray photoelectron spectroscopy (XPS) was performed by using a Thermo Scientific Escalab 250Xi spectrometer. The specific surface area (SSA) was determined via using methylene blue (MB) adsorption method on a UV-vis spectrophotometer (UV-5100, Anhui Wanyi; Tran et al., 2015), the SSA of g-C_3N_4 and g-C_3N_4/MS were calculated by the following equation:

$$SSA = \frac{N_A A_{MB}(C_0 - C_e)V}{M_{MB}m_s}$$

Where N_A represents Avogadro's constant (6.02×10^{23} mol^{-1}), A_{MB} represents the covered area of per MB molecule (typically assumed to be 1.35 nm^2), C_o and C_e are the initial and equilibrium concentrations of MB, V is the volume of MB solution, M_{MB} is the relative molecular mass of MB, and m_s is the mass of the sample.

Evaluation of Photocatalytic Activity

The photocatalytic activity of g-C_3N_4/MS was evaluated in both gaseous systems. Photocatalytic removal of NO at ppb level was previously reported in details (Zhang et al., 2014). Typically, A 150 W metal halide lamp with a visible light filter (>420 nm) was employed to operate the experiment. A piece of g-C_3N_4/MS was put into the reactor for photocatalytic activity test. The light intensity is 35.88 mW cm^{-2} measured by a light intensity meter. The initial concentration of NO was diluted to 500 ppb by drying air. The flow rates of dry air and NO are set at 2 L min^{-1} and 9.5 mL min^{-1}, respectively. The formula of degradation rate of NO was counted by the following equation:

$$\omega\,(\%) = \frac{[C\,(NO_X) - C\,(NO) - C_0(NO_2)]}{C\,(NO_X)} \times 100\%$$

Where C (NO_x) represents the concentration of total nitric oxide (NO_2 and NO), while C_0 is the initial concentration of NO_2 when reaching the adsorption-desorption equilibrium.

The photocatalytic reduction of CO_2 was performed in a 380 mL home-made reactor at ambient temperature and pressure. A 300 W Xe lamp was used as a light source and positioned 8 cm above the photocatalytic reactor. In a typical test, a plastic beaker with 20 mL deionized water was deposited at the bottom of the reactor, and a culture dish with 100 mg g-C_3N_4 powder or g-C_3N_4/MS (38.5 cm^2) was placed on the plastic beaker. Before irradiation, the reactor was sealed and vacuumed by a pump, then removed air by blowing argon for 15 min. Subsequently, 1 mL CO_2 was injected into the reactor. After 4 h irradiation, 1 mL of gas was taken out from the reactor and analyzed by using a gas chromatograph (Techcomp GC7900)

equipped with a flame ionized detector (FID) and a thermal conductivity detector (TCD). CO and CH_4 were analyzed by the FID, and H_2 was analyzed by TCD.

RESULTS AND DISCUSSION

Fabrication and Physical Properties of g-C_3N_4/MS

The general preparation approach of g-C_3N_4/MS was illustrated in **Figure 1A**. Direct mixture of powdery g-C_3N_4 and MS is hard to gain a monolithic g-C_3N_4/MS with good particle dispersion and well contact between particle and MS skeleton. Therefore, the g-C_3N_4 powder was firstly added into water and sonicated for 30 min to form uniform suspension, which make the particle diffusion easy and fast in the porous structure of MS. Then, the pretreated MS was immersed into this suspension through dipping and squeezing procedures until MS was fully covered by g-C_3N_4 particles. Finally, followed by a conventional freezing-drying process, the monolithic g-C_3N_4/MS was obtained. Obviously, no large particles were observed on the cross-section photo in **Figure 1A**, indicating that the g-C_3N_4 powder was uniformly coated on MS skeleton. For comparison, we also dipped MS in a saturated solution of urea, which is the g-C_3N_4 precursor. After removing the water by freeze-drying, we attempted to fabricate the monolithic g-C_3N_4/MS by *in-situ* immobilizing approach at 550°C. However, the obtained monolithic composite became very fragile due to the carbonization of MS skeleton. Moreover, the g-C_3N_4 powder gathered on the composite surface with an inhomogeneous dispersion (Figure S1). The failed trial illustrated the mild ultrasonic-coating approach is superior to other methods for monolithic g-C_3N_4/MS fabrication. Importantly, the facile ultrasonic-coating approach developed here is also adapted to other porous supports, such as nickel foam, Al_2O_3 ceramic foam, glass fiber and polyester fiber, and the corresponding monolithic products of g-C_3N_4 are shown in Figure S2.

Physical properties of materials are pivotal to their practical application. As shown in **Figure 1B**, the monolithic g-C_3N_4/MS has an ultra-low density (11.5 mg cm^{-3}), which can stay on dog tail grass and remarkably lighter than that of reported BiOBr/reduced GOA (50 mg cm^{-3}) (Liu W. J. et al., 2015), TiO_2/graphene aerogel (19 mg cm^{-3}) (Qiu et al., 2014), and MoS_2/reduced GOA (56.1 mg cm^{-3}) (Zhang R. Y. et al., 2017). Moreover, SSA of g-C_3N_4/MS (7.6 m^2 g^{-1}) is much more larger than that of the pristine g-C_3N_4 (0.9 m^2 g^{-1}), which not only offer more active sites but also have larger absorption capacity than its powdery counterpart. In addition, facile modification of shapes and sizes endows g-C_3N_4/MS with a good flexibility to handle different situations in practical application (**Figures 1C,D**). More importantly, the g-C_3N_4/MS presents excellent elasticity. As revealed in **Figure 1E**, the g-C_3N_4/MS can instantaneously recover and maintain its integrity after removing of the heavy loading (410 g counterweight), suggesting that g-C_3N_4/MS possesses enough mechanical strength to deal with intricate operation in environmental abatement. To further ensure the firmness of g-C_3N_4 on MS skeletons, a test is carried
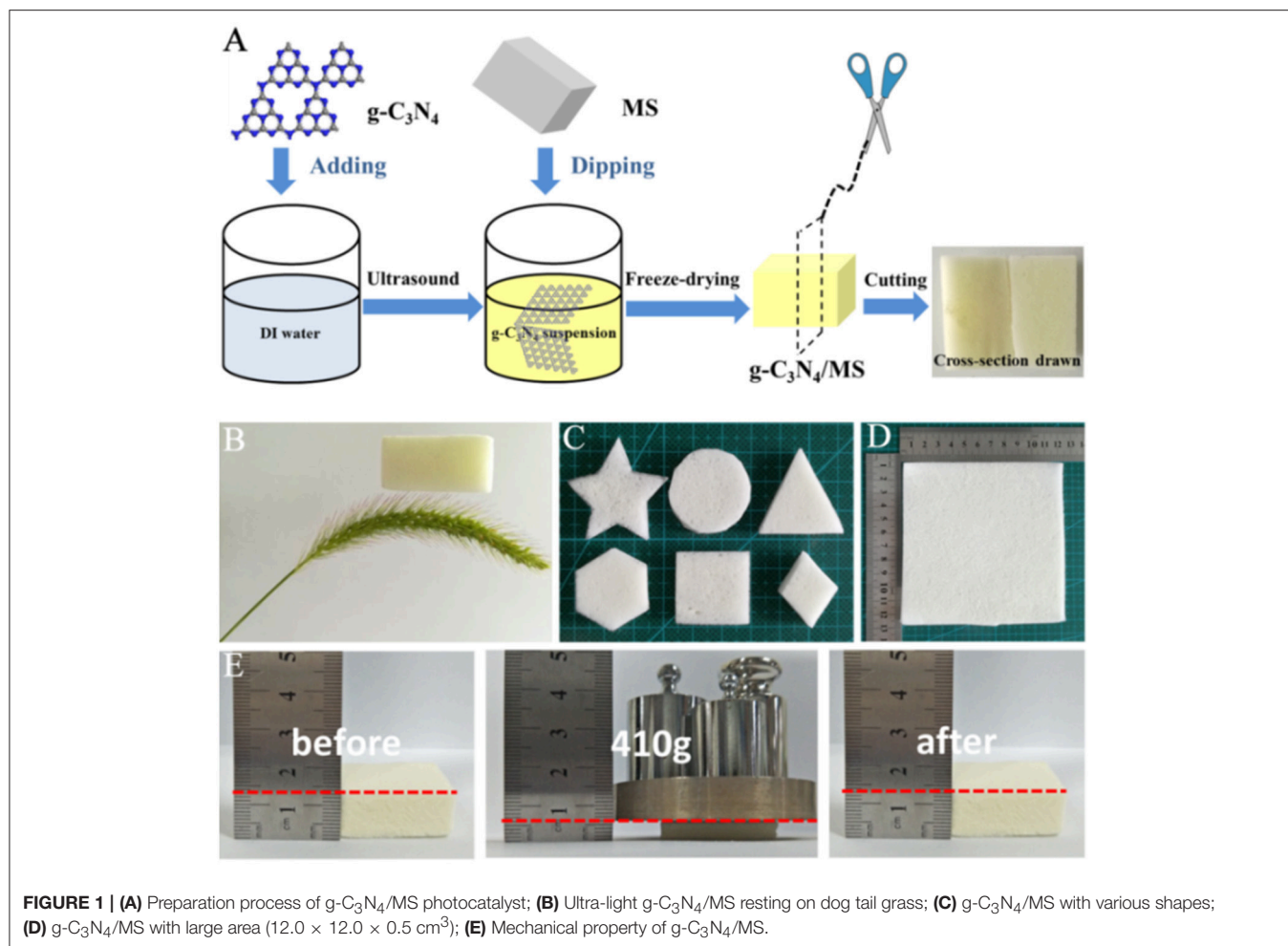
FIGURE 1 | (A) Preparation process of g-C_3N_4/MS photocatalyst; **(B)** Ultra-light g-C_3N_4/MS resting on dog tail grass; **(C)** g-C_3N_4/MS with various shapes; **(D)** g-C_3N_4/MS with large area (12.0 × 12.0 × 0.5 cm^3); **(E)** Mechanical property of g-C_3N_4/MS.

out by blowing the g-C_3N_4/MS with a strong airflow for 12 h, the detailed simulation device diagram is shown in Figure S3a. The dropping g-C_3N_4 powder from g-C_3N_4/MS is collected and weighted up. The final weight loss is less than 7.60 mg, which account for 1.15% of g-C_3N_4 loaded on MS skeletons (Figure S3b). The above result demonstrates that g-C_3N_4 is firmly distributed on MS even under extreme work condition, which is pivotal to the recycle in practical application.

Photocatalytic Activity

Benefit from the characteristics of low-density, high porosity and good elasticity, the monolithic g-C_3N_4/MS can be used to removal gaseous pollutants. Therefore, two different photocatalysis applications including NO removal, dye degradation, and CO_2 photoreduction, are selected to test the photocatalytic activity of the as-prepared monolithic g-C_3N_4/MS. NO, a typical air contaminants, mostly produced from the combustion of fossil fuels and the emission of vehicle exhaust, can cause a series of atmosphere pollution problems such as acid rain, photochemical smog and haze (Wang et al., 2016). Photo-oxidation technique is considered an alternative to remove NO at low concentration (Zhou et al., 2014).

Therefore, the g-C_3N_4/MS samples are firstly investigated by NO removal at the indoor ppb level. **Figure 2A** shows the effect of g-C_3N_4 concentration on NO photo-removal ratio occurring on g-C_3N_4/MS. Notably, the MS coated with 5 mg mL^{-1} suspension achieves the highest removal ratio of 45% within 30 min. As the concentration of g-C_3N_4 suspension less than 5 mg mL^{-1}, the photocatalytic activity of g-C_3N_4/MS gradually enhanced with the increased concentration of g-C_3N_4 suspension. With a concentration higher than 5 mg mL^{-1}, the photocatalytic activity of the g-C_3N_4/MS slightly decreased, attributing to agglomeration of the excessive g-C_3N_4 which not only hinder the NO transport by blocking pore channels in MS, but also cause a reduced light transmittance. Moreover, the thicknesses of MS have also been investigated, which is closely associated with the light utilization. Benefit from the good transparence of MS, the activity of g-C_3N_4/MS enhanced along with increased MS thickness in **Figure 2B**, but the corresponding best unit mass rate constant (0.868 min^{-1} g^{-1}) of NO removal is belong to g-C_3N_4/MS with 0.5 cm thickness (As shown in Figure S4). Based on above results, the optimal concentration and thickness were fixed at 5 mg mL^{-1} and 0.5 cm, respectively.
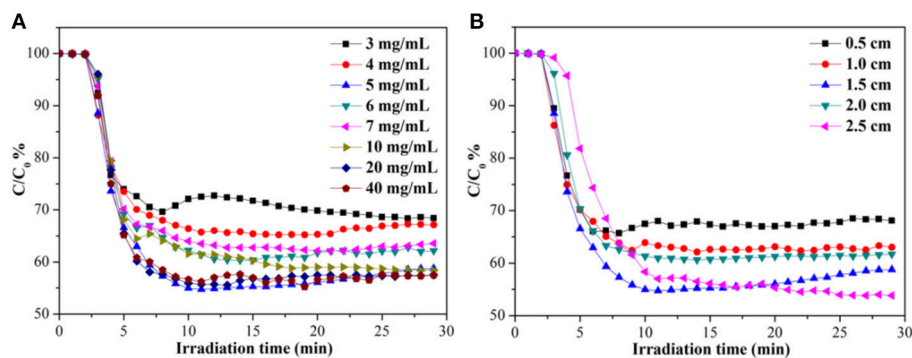
FIGURE 2 | Photocatalytic NO removal ratios in presence of g-C$_3$N$_4$/MS fabricated with **(A)** different concentrations and **(B)** different thicknesses under visible light irradiation.
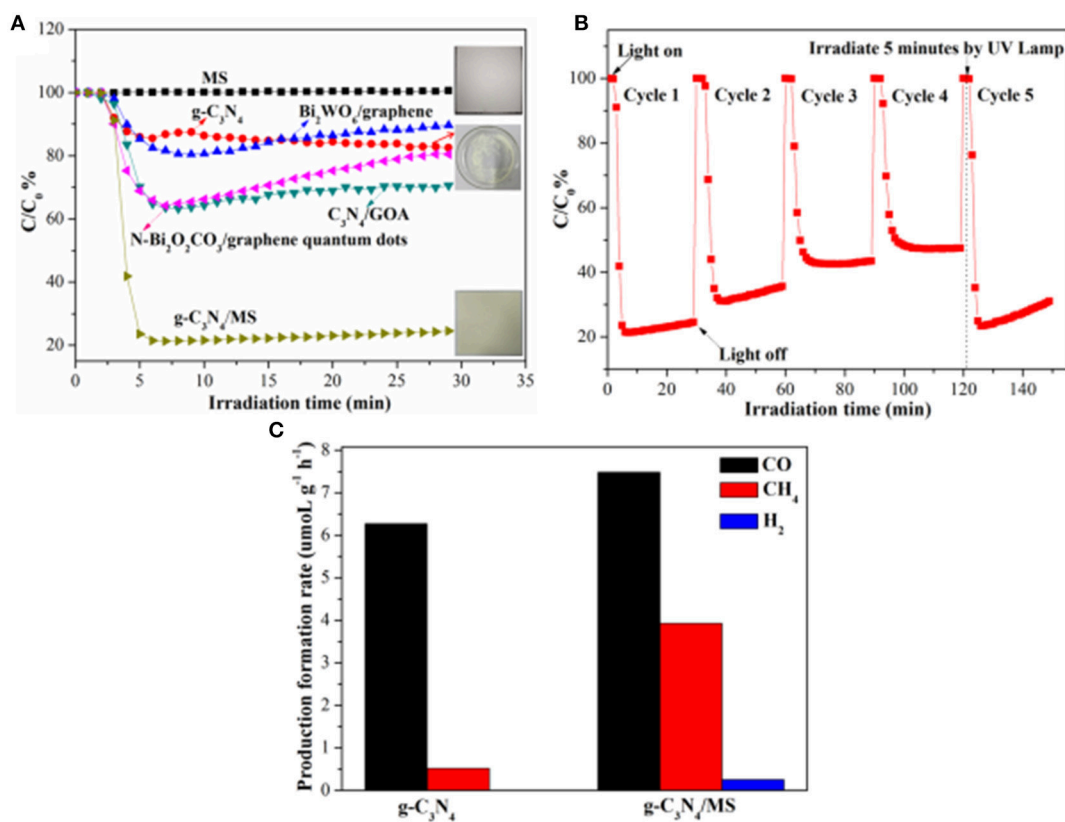
FIGURE 3 | Photocatalytic activity of g-C$_3$N$_4$/MS under visible-light irradiation: **(A)** NO removal ratios of different samples; **(B)** Photocatalytic recycling test on large area g-C$_3$N$_4$/MS; **(C)** Production rate of CO, CH$_4$ and H$_2$ on g-C$_3$N$_4$, g-C$_3$N$_4$/MS respectively in photocatalytic CO$_2$ reduction under UV-Vis light irradiation.

The fabrication and utilization of monolithic photocatalysts with large area on macro-scale is significant to their practical application. Therefore, a monolithic g-C$_3$N$_4$/MS with area of 12.0×12.0 cm^2 is prepared for further test of NO removal under visible-light illumination (**Figure 3A**). For comparison, the NO removal on powdery g-C$_3$N$_4$ and pristine MS are also performed under the same conditions, respectively. Surprisingly, monolithic g-C$_3$N$_4$/MS presents the highest NO removal ratio of 78.6% in initial 5 min which is about 4.5 times higher than

that of powdery g-C$_3$N$_4$ (17.6%), while no NO removal occurs on the pristine MS. After initial 5 min, NO removal ratio of g-C$_3$N$_4$/MS tends to be steady, which could be interpreted as partial active sites replaced by adsorptive NO$_3^-$ or NO (Ai et al., 2009; Huang et al., 2010; Liu et al., 2017) and finally reached an adsorption and desorption equilibrium of these oxynitrides. Moreover, comparison with other photocatalysts in our previous work, large area g-C$_3$N$_4$/MS exhibits optimum activity (78.6%), which is approximate 4.25, 2.25 and 2.32 times higher than

that of Bi_2WO_6/graphene (Zhou et al., 2014), C_3N_4/GOA (GOA) (Wan et al., 2016), and N-$Bi_2O_2CO_3$/graphene quantum dots (Liu et al., 2017), respectively. Notably, the fraction of generated NO_2 is lower than 5.4% over all our samples (as shown in Figure S5a), indicating those samples selectively oxidize NO to NO_3^- rather than NO_2. Based on above results, the g-C_3N_4/MS with large area shows obviously enhanced photocatalytic activity than its powdery counterpart, indicating the monolithic photocatalyst is an effective strategy to solve the problems encountered by powdery photocatalysts in large-scale application.

The stability and recyclability of photocatalysts are also important to their practical applications (Hu et al., 2017). Here, we carried out cycle and long-time tests to further evaluate the performance of the monolithic g-C_3N_4/MS. The result of cycle test is listed in **Figure 3B**. It can be seen that the NO removal ratio of g-C_3N_4/MS dropped quickly during the first two cycles. After that, the NO removal ratio approached to stabilization within third cycle and slightly decreased with incremental cycle-index, which attributed to temporary absorption equilibrium of oxynitrides (NO, NO_3^-) in third cycle and their continuous accumulation on g-C_3N_4/MS. Fortunately, after UV lamp irradiation for 5 min, the adsorbed oxynitrides are desorbed and results in an immediate recovery of sample activity (**Figure 3B**). Furthermore, result of long-time test is displayed in Figure S5b. The g-C_3N_4/MS can achieve a stable catalytic performance after 1 h and keep a relatively high activity in the 2 h test interval. All above results confirm that the large area g-C_3N_4/MS has a superior recyclability and stability for NO removal, confirming its potential in practical application.

Apart from the photo-oxidation availability, the monolithic g-C_3N_4/MS also exhibits good ability of CO_2 photoreduction. CO_2 is the main greenhouse gas that generation from human activity and the combustion of fossil fuels which is responsible for global warming (Norby and Luo, 2004). As displayed in **Figure 3C**, the g-C_3N_4/MS shows higher photocatalytic activity (7.48 μmol g^{-1} h^{-1} CO, 3.93 μmol g^{-1} h^{-1} CH_4 and 0.26 μmol g^{-1} h^{-1} H_2) than that of powdery g-C_3N_4 (6.27 μmol g^{-1} h^{-1} CO, 0.52 μmol g^{-1} h^{-1} CH_4 and 0 μmol g^{-1} h^{-1} H_2). Notably, yield of CO is higher than that of CH_4 on both two samples, because the conversion from CO_2 to CO is 4-electron process, whereas that from CO_2 to CH_4 is 8-electrons process, obviously, the former is easier than the latter which can account for higher yield of CO. No H_2 generated on g-C_3N_4 and traced H_2 appeared on g-C_3N_4/MS indicate that all samples have high selectivity for CO_2 reduction rather than H_2 reduction.

In view of above results of NO removal, and CO_2 photoreduction, the monolithic g-C_3N_4/MS does show practical potential in various applications and enhanced photocatalytic activity than its powdery counterpart. The large SAA must be responsible for this activity enhancement. However, to get a deep insight into the reasons of the improved performance, more investigations further carried out on the monolithic g-C_3N_4/MS.

Structure and Morphology

The PXRD patterns of MS, g-C_3N_4/MS, sonicated g-C_3N_4 and g-C_3N_4 are displayed in **Figure 4**. The peaks at ca. 13.1 and 27.3° can be assigned to (100) and (002) crystal planes of g-C_3N_4, respectively (Gholipour et al., 2016). Obviously, the PXRD patterns of g-C_3N_4 are consistent before and after ultrasonic process, confirming the crystal structure of g-C_3N_4 is very stable. Moreover, no difference is found in the PXRD patterns of g-C_3N_4/MS and MS, indicating the g-C_3N_4 particles are uniformly dispersed on the porous framework of MS rather than aggregated on its surface.

To reveal the microstructure and morphology of samples, TEM and SEM were conducted as shown in **Figure 5**. The TEM images of g-C_3N_4 and sonicated g-C_3N_4 show similar thin nano-flake structure with some mesopores (**Figures 5A,B**), which derived from gases releasing such as NH_3 and CO_2 during the pyrolysis of urea (Mao et al., 2013). Combination with PXRD results, it is sure no noticeable change appeared on the structure and morphology of g-C_3N_4 before and after the ultrasonic. In **Figure 5C**, the SEM image of MS reveals an interconnected 3D network structure with abundant open-cell pores, which not only offer sufficient channels for reactant transport, but also offer enough locations for photocatalyst particle dispersion. It is notable that the g-C_3N_4 was successfully coated on the smooth skeleton of MS according to the g-C_3N_4/MS image in **Figure 5D**. Based on the analysis of structure and morphology, the uniform dispersion of g-C_3N_4 achieves in monolithic g-C_3N_4/MS, confirming the feasibility of our coating strategy.

Figure 6 shows the FT-IR spectra of g-C_3N_4, g-C_3N_4/MS and MS. The spectrum of g-C_3N_4 displays typical peaks at 3000-3600 cm^{-1}, 1200-1700 cm^{-1}, and 811 cm^{-1}, which are ascribed to the vibrational absorption of N-H and O-H, CN heterocycles and triazine unit (Kang et al., 2015; Wei et al., 2016; Sun Z. X. et al., 2017). Moreover, in the spectrum of MS, the prominent
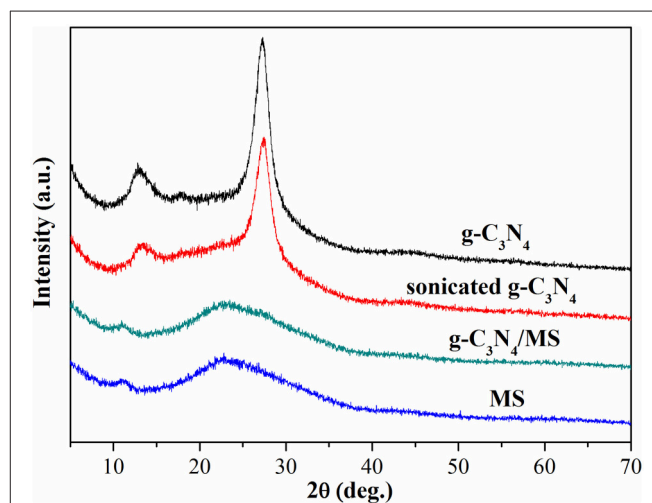
FIGURE 4 | PXRD patterns of g-C_3N_4, sonicated g-C_3N_4, g-C_3N_4/MS and MS.
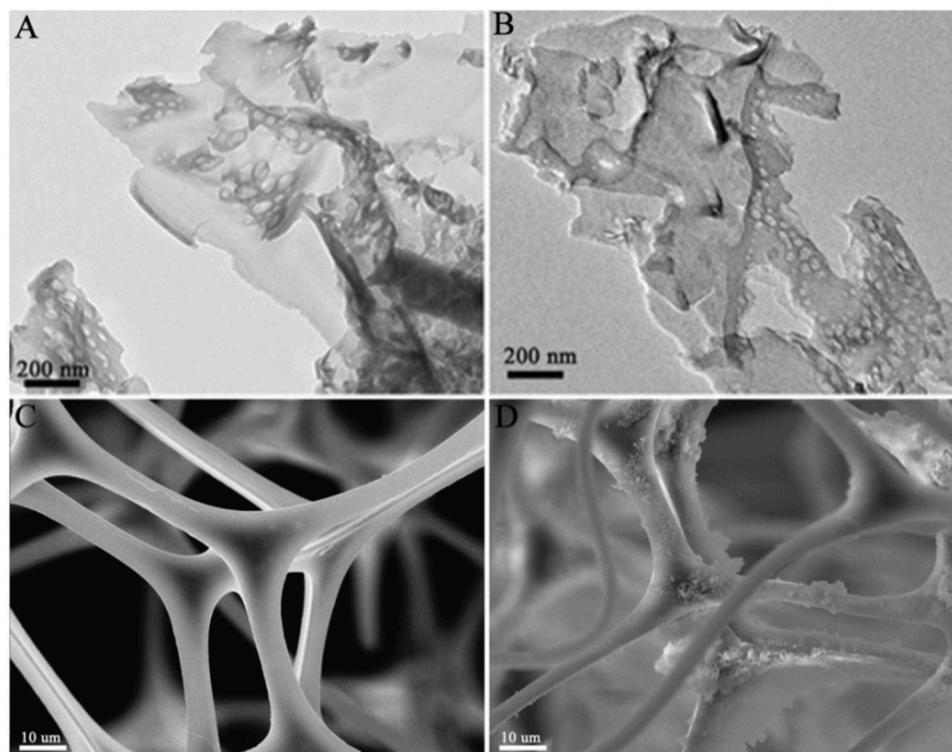
FIGURE 5 | TEM images of samples: **(A)** g-C_3N_4; **(B)** sonicated g-C_3N_4. SEM images of samples: **(C)** MS; **(D)** g-C_3N_4/MS.
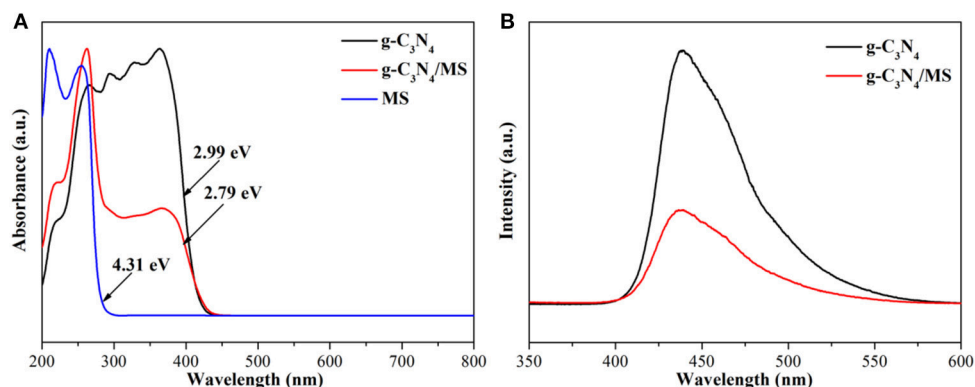
FIGURE 7 | **(A)** UV-vis DRS of g-C3N4, g-C3N4/MS and MS; **(B)** PL spectra of g-C3N4, g-C3N4/MS.

peaks located at 808, 1154, 1545, and 3422 cm^{-1}, attributing to triazine ring bending, C-O stretching, C=N stretching and N-H stretching, while peaks centered at 988, 1329, and 1466 cm^{-1} corresponding to C-H bending vibrations (Pham and Dickerson, 2014; Zhang W. B. et al., 2017). Particularly, a new peak and an intensive peak appeared at 1334 cm^{-1} and 813 cm^{-1} in g-C_3N_4/MS spectrum, indicating a weak chemical interaction exists between g-C_3N_4 and MS skeletons. The above results reveal both van der waals and chemical interactions between g-C_3N_4 and MS, which explain the good firmness of monolithic g-C_3N_4/MS.

Band Structure and Photocatalytic Mechanism

The band gap of MS, g-C_3N_4 and g-C_3N_4/MS were determined by the results of UV-vis DRS in **Figure 7A**. Obviously, g-C_3N_4 absorption is located in visible region with a calculated band gap of 2.99 eV, while MS shows only UV light absorption with a wide band gap of 4.31 eV. Moreover, the DRS profile of the g-C_3N_4/MS exhibits a mechanical combination of the absorption features of the g-C_3N_4 and MS alone. Importantly, visible-light absorption of g-C_3N_4/MS gets a slight enhancement (2.79 eV), which may be attributed to the light multistage
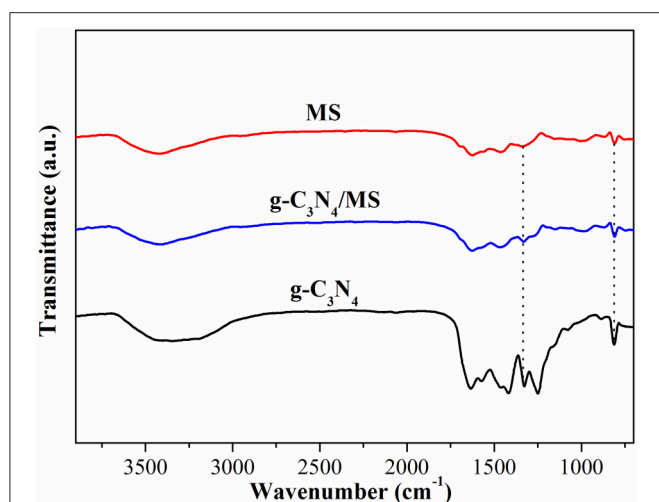
FIGURE 6 | FTIR spectra of g-C3N4, g-C3N4/MS and MS.
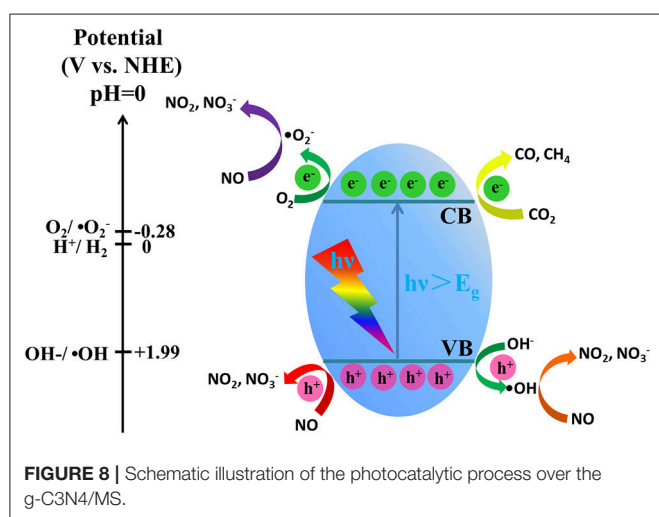
FIGURE 8 | Schematic illustration of the photocatalytic process over the g-C3N4/MS.

refraction and reflection on the MS framework (Dong et al., 2014b). In addition, the g-C_3N_4/MS not only enhances the light absorption, but also significantly suppresses the recombination of photo-generated carriers according to photoluminescence (PL) spectra in **Figure 7B**, which accounts for the enhancement of photocatalytic activity.

According to the above UV-vis DRS analysis (**Figure 7A**) and the XPS valence band spectrum (Figure S6), the band structure of g-C_3N_4/MS is proposed in **Figure 8** with VB edge and CB edge located at 2.01 and -0.98 eV, respectively. As shown in **Figure 8**, the potential of VB holes (h^+) is slight positive than OH^-/OH (1.99 eV), while the potential of CB electron (e^-) is much negative than that of O_2/O_2^- (-0.28 eV). Therefore, the photogenerated holes can directly oxidize OH^- to OH, and the photogenerated electrons can reduce easily O_2 to O_2^-. It is well known that OH and O_2^- usually have strong oxidative ability and play the key role in photocatalytic oxidation reaction (Huang et al., 2015b,c, 2017b). Moreover, in consideration of the oxidation potentials of NO2/NO (1.03 eV), HNO2/NO

(0.99 eV), HNO3/NO (0.94 eV) (Wan et al., 2016), all OH, O_2^- and hole generated on g-C_3N_4/MS are able to remove NO. In addition, the reduction potentials of E (CO_2/CH_4), E (CO_2/CO) and E (H_2O/H_2) were located at -0.24, -0.52, and -0.41 eV, respectively (Yu et al., 2014; Han B. et al., 2015). Comparison with CB potential (-0.98 eV), the photogenerated electron is capable of reducing CO_2 on g-C_3N_4/MS. Based on above analyses and the results in photocatalytic activity part, the possible photocatalytic mechanism are simply illustrated in **Figure 8**. In short, there are three main pathways for NO removal, involving three different active oxidation species (OH, O_2^- and h^+), while there is one pathway for CO_2 photoreduction, involving only one active species (e^-).

CONCLUSIONS

In summary, a novel monolithic g-C_3N_4/MS was fabricated by a facile ultrasonic-coating method. This monolithic g-C_3N_4/MS possesses a uniform dispersion of g-C_3N_4 and large SSA, which not only facilitate exposing more active sites of g-C_3N_4 but also enhancing the visible-light absorption. Consequently, monolithic g-C_3N_4/MS shows obviously improved visible-light photocatalytic activity. The PL detection further reveals that enhanced separation of photogenerated carriers is also responsible for the activity enhancement. More importantly, the characteristics of low-density and high porosity allow the monolithic g-C_3N_4/MS to be applied in various environmental issues, while the high elasticity, good firmness, and mechanical strength give it noticeable recyclability and stability, confirming its feasibility for practical application. All in all, in this work, we fabricated a monolithic g-C_3N_4/MS with enhanced photocatalytic activity which can be easy to achieve large-scale production for practical photocatalysis application. Our results provide a low-cost and mild method for mass production of new monolithic photocatalysts.

AUTHOR CONTRIBUTIONS

YY: Partly designed the experiments and wrote the manuscript; RZ, TR, and WW: Assisted in the analysis and interpretation of the data; YZ and QZ: Proposed the project, designed the experiment, and wrote the manuscript.

ACKNOWLEDGMENTS

SUPPLEMENTARY MATERIAL

The Supplementary Material for this article can be found online at: https://www.frontiersin.org/articles/10.3389/fchem.2018.00156/full#supplementary-material

REFERENCES

Ai, Z. H., Ho, W. K., Lee, S. C., and Zhang, L. Z. (2009). Efficient photocatalytic removal of NO in indoor air with hierarchical bismuth oxybromide nanoplate microspheres under visible light. *Environ. Sci. Technol.* 43, 4143–4150. doi: 10.1021/es9004366

Cheng, F. X., Wang, H. N., and Dong, X. P. (2015). The amphoteric properties of g-C3N4 nanosheets and fabrication of their relevant heterostructure photocatalysts by an electrostatic re-assembly route. *Chem. Commun.* 51, 7176–7179. doi: 10.1039/C5CC01035G

Cheng, W., Rechberger, F., and Niederberger, M. (2016). From 1D to 3D–macroscopic nanowire aerogel monoliths. *Nanoscale* 8, 14074–14077. doi: 10.1039/C6NR04429H

Cui, C., Li, S., Qiu, Y. W., Hu, H. H., Li, X. Y., and Li, C. R. (2017). Fast assembly of Ag3PO4 nanoparticles within three-dimensional graphene aerogels for efficient photocatalytic oxygen evolution from water splitting under visible light. *Appl. Catal. B Environ.* 200, 666–672. doi: 10.1016/j.apcatb.2016.07.056

Dong, F., Ou, M. Y., Jiang, Y. K., Guo, S., and Wu, Z. B. (2014a). Efficient and durable visible light photocatalytic performance of porous carbon nitride nanosheets for air purification. *Ind. Eng. Chem. Res.* 53, 2318–2330. doi: 10.1021/ie4038104

Dong, F., Wang, Z. Y., Li, Y. H., Ho, W. K., and Lee, S. C. (2014b). Immobilization of polymeric g-C3N4 on structured ceramic foam for efficient visible light photocatalytic air purification with real indoor illumination. *Environ. Sci. Technol.* 48, 10345–10353. doi: 10.1021/es502290f

Fan, Y., Ma, W., Han, D., Gan, S., Dong, X., and Niu, L. (2015). Convenient recycling of 3D AgX/graphene aerogels (X= Br, Cl) for efficient photocatalytic degradation of water pollutants. *Adv. Mater.* 27, 3767–3773. doi: 10.1002/adma.201500391

Gholipour, M. R., Béland, F., and Do, T. O. (2016). Post-calcined carbon nitride nanosheets as an efficient photocatalyst for hydrogen production under visible light irradiation. *ACS Sustain. Chem. Eng.* 5, 213–220. doi: 10.1021/acssuschemeng.6b01282

Han, B., Wei, W., Chang, L., Cheng, P. F., and Hu, Y. H. (2015). Efficient visible light photocatalytic CO2 reforming of CH4. *ACS Catal.* 6, 494–497. doi: 10.1021/acscatal.5b02653

Han, Q., Wang, B., Zhao, Y., Hu, C., and Qu, L. (2015). A Graphitic-C3N4 "Seaweed" architecture for enhanced hydrogen evolution. *Angew. Chem. Int. Ed.* 54, 11433–11437. doi: 10.1002/anie.201504985

Hossain, S. T., and Mukherjee, S. K. (2013). Toxicity of cadmium sulfide (CdS) nanoparticles against *Escherichia coli* and HeLa cells. *J. Hazard. Mater.* 260, 1073–1082. doi: 10.1016/j.jhazmat.2013.07.005

Hou, Y., Zuo, F., Dagg, A. P., Liu, J. K., and Feng, P. Y. (2014). Branched WO3 nanosheet array with layered C3N4 heterojunctions and CoOx nanoparticles asa flexible photoanode for efficient photoelectrochemical water oxidation. *Adv. Mater.* 26, 5043–5049. doi: 10.1002/adma.201401032

Hu, J. D., Chen, D. Y., Li, N. J., Xu, Q. F., Li, H., He, J. H., et al. (2017). *In situ* fabrication of Bi2O2CO3/MoS2 on carbon nanofibers for efficient photocatalytic removal of NO under visible-light irradiation. *Appl. Catal. B Environ.* 217, 224–231. doi: 10.1016/j.apcatb.2017.05.088

Huang, H. W., Han, X., Li, X., Wang, S., Chu, P. K., and Zhang, Y. (2015a). Fabrication of multiple heterojunctions with tunable visible-light-active photocatalytic reactivity in BiOBr–BiOI full-range composites based on microstructure modulation and band structures. *ACS Appl. Mater. Interfaces* 7, 482–492. doi: 10.1021/am5065409

Huang, H. W., He, Y., Lin, Z. S., Kang, L., and Zhang, Y. H. (2013). Two novel Bi-based borate photocatalysts: crystal structure, electronic structure, photoelectrochemical properties, and photocatalytic activity under simulated solar light irradiation. *J. Phys. Chem. C* 117, 22986–22994. doi: 10.1021/jp4084184

Huang, H. W., He, Y., Li, X. W., Li, M., Zeng, C., Dong, F., et al. (2015b). Bi2O2(OH)(NO3) as a desirable [Bi2O2]2+ layered photocatalyst: strong intrinsic polarity, rational band structure and {001} active facets co-beneficial for robust photooxidation capability. *J. Mater. Chem. A* 3, 24547–24556. doi: 10.1039/C5TA07655B

Huang, H. W., Li, X. W., Wang, J. J., Dong, F., Chu, P. K., Zhang, T. R., et al. (2015c). Anionic group self-doping as a promising strategy: band-gap engineering and multi-functional applications of high-performance CO3²⁻ doped Bi2O2CO3. *ACS Catal.* 5, 4094–4103. doi: 10.1021/acscatal.5b00444

Huang, H. W., Xiao, K., He, Y., Zhang, T. R., Dong, F., Du, X., et al. (2016). *In situ* assembly of BiOI@Bi12O17Cl2 p-n junction: charge induced unique front-lateral surfaces coupling heterostructure with high exposure of BiOI {001} active facets for robust and nonselective photocatalysis. *Appl. Catal. B Environ.* 199, 75–86. doi: 10.1016/j.apcatb.2016.06.020

Huang, H. W., Tu, S. C., Zeng, C., Zhang, T. R., Reshak, A. H., and Zhang, Y. H. (2017a). Macroscopic polarization enhancement promoting photo⁻ and piezoelectric⁻ induced charge separation and molecular oxygen activation. *Angew. Chem.* 39, 12022–12026. doi: 10.1002/ange.201706549

Huang, H. W., Xiao, K., Zhang, T. R., Dong, F., and Zhang, Y. H. (2017b). Rational design on 3D hierarchical bismuth oxyiodides via *in situ* self-template phase transformation and phase-junction construction for optimizing photocatalysis against diverse contaminants. *Appl. Catal. B Environ.* 203, 879–888. doi: 10.1016/j.apcatb.2016.10.082

Huang, Y., Ai, Z. H., Ho, W. K., Chen, M. J., and Lee, S. C. (2010). Ultrasonic spray pyrolysis synthesis of porous Bi2WO6 microspheres and their visible-light-induced photocatalytic removal of NO. *J. Phys. Chem. C* 114, 6342–6349. doi: 10.1021/jp912201h

Kang, S. F., Fang, Y., Huang, Y. K., Cui, L. F., Wang, Y. Z., Qin, H. F., et al. (2015). Critical influence of g-C3N4 self-assembly coating on the photocatalytic activity and stability of Ag/AgCl microspheres under visible light. *Appl. Catal. B Environ.* 168, 472–482. doi: 10.1016/j.apcatb.2015.01.002

Li, P. H., Wang, F., Wei, S. Q., Li, X. Y., and Zhou, Y. (2017). Mechanistic insights into CO2 reduction on Cu/Mo-loaded two-dimensional g-C3N4 (001). *Phys. Chem. Chem. Phys.* 19, 4405–4410. doi: 10.1039/C6CP08409E

Liang, Q., Li, Z., Yu, X., Huang, Z. H., Kang, F., and Yang, Q. H. (2015). Macroscopic 3D porous graphitic carbon nitride monolith for enhanced photocatalytic hydrogen evolution. *Adv. Mater.* 27, 4634–4639. doi: 10.1002/adma.201502057

Lin, Z. Y., Li, J. L., Zheng, Z. Q., Li, L. H., Yu, L. L., Wang, C. X., et al. (2016). A floating sheet for efficient photocatalytic water splitting. *Adv. Energy Mater.* 6:1600510. doi: 10.1002/aenm.201600510

Liu, G., Niu, P., Sun, C. H., Smith, S. C., Chen, Z. G., Lu, G. Q., et al. (2010). Unique electronic structure induced high photoreactivity of sulfur-doped graphitic C3N4. *J. Am. Chem. Soc.* 132, 11642–11648. doi: 10.1021/ja103798k

Liu, G., Zhao, Y. N., Sun, C. H., Li, F., Lu, G. Q., and Cheng, H. M. (2008). Synergistic effects of B/N doping on the visible-light photocatalytic activity of mesoporous TiO2. *Angew. Chem. Int. Ed.* 47, 4516–4520. doi: 10.1002/anie.200705633

Liu, J. H., Zhang, T. K., Wang, Z. C., Dawson, G., and Chen, W. (2011). Simple pyrolysis of urea into graphitic carbon nitride with recyclable adsorption and photocatalytic activity. *J. Mater. Chem.* 21, 14398–14401. doi: 10.1039/c1jm12620b

Liu, T. T., Zhao, G. Z., Zhang, W. H., Chi, H. J., Hou, C. L., and Sun, Y. Y. (2015). The preparation of superhydrophobic graphene/melamine composite sponge applied in treatment of oil pollution. *J. Porous Mater.* 22, 1573–1580. doi: 10.1007/s10934-015-0040-8

Liu, W. J., Cai, J. Y., and Li, Z. H. (2015). Self-assembly of semiconductor nanoparticles/reduced graphene oxide (RGO) composite aerogels for enhanced photocatalytic performance and facile recycling in aqueous photocatalysis. *ACS Sustain. Chem. Eng.* 3, 277–282. doi: 10.1021/sc5006473

Liu, Y., Yu, S., Zhao, Z. Y., Dong, F., Dong, X. A., and Zhou, Y. (2017). N-Doped Bi2O2CO3/graphene quantum dot composite photocatalyst: enhanced visible-light photocatalytic no oxidation and in situ drifts studies. *J. Phys. Chem. C* 121, 12168–12177. doi: 10.1021/acs.jpcc.7b02285

Maggos, T., Bartzis, J. G., Leva, P., and Kotzias, D. (2007). Application of photocatalytic technology for NOx removal. *Appl. Phys. A* 89, 81–84. doi: 10.1007/s00339-007-4033-6

Mao, J., Peng, T. Y., Zhang, X. H., Li, K., Ye, L. Q., and Zan, L. (2013). Effect of graphitic carbon nitride microstructures on the activity and selectivity of photocatalytic CO2 reduction under visible light. *Catal. Sci. Technol.* 3, 1253–1260. doi: 10.1039/c3cy20822b

Norby, R. J., and Luo, Y. Q. (2004). Evaluating ecosystem responses to rising atmospheric CO2 and global warming in a multi-factor world. *New Phytol.* 162, 281–293. doi: 10.1111/j.1469-8137.2004.01047.x

Pham, V. H., and Dickerson, J. H. (2014). Superhydrophobic silanized melamine sponges as high efficiency oil absorbent materials. *ACS Appl. Mater. Interfaces* 6, 14181–14188. doi: 10.1021/am503503m

Qiu, B. C., Xing, M. Y., and Zhang, J. L. (2014). Mesoporous TiO_2 nanocrystals grown in situ on graphene aerogels for high photocatalysis and lithium-ion batteries. *J. Am. Chem. Soc.* 136, 5852–5855. doi: 10.1021/ja500873u

Sun, H., Zhou, X. Z., Zhang, H. Z., and Tu, W. X. (2017). An efficient exfoliationmethod to obtain graphitic carbon nitride nanosheets with superior visible-light photocatalytic activity. *Int. J. Hydrogen Energy* 42, 7930–7937. doi: 10.1016/j.ijhydene.2016.12.080

Sun, Z. X., Fischer, J. M. T. A., Li, Q., Hu, J., Tang, Q. J., Wang, H. Q., et al. (2017). Enhanced CO_2 photocatalytic reduction on alkali-decorated graphitic carbon nitride. *Appl. Catal. B Environ.* 216, 146–155. doi: 10.1016/j.apcatb.2017.05.064

Tang, L., Jia, C. T., Xue, Y. C., Li, L., Wang, A. Q., Xu, G., et al. (2017). Fabrication of compressible and recyclable macroscopic g-C_3N_4/GO aerogel hybrids for visible-light harvesting: a promising strategy for water remediation. *Appl. Catal. B Environ.* 219, 241–248. doi: 10.1016/j.apcatb.2017.07.053

Tran, D. N. H., Kabiri, S., Sim, T. R., and Losic, D. (2015). Selective adsorption of oil-water mixtures using polydimethylsiloxane (PDMS)-graphene sponges. *Environ. Sci. Water Res. Technol.* 1, 298–305. doi: 10.1039/C5EW00035A

Wan, W. C., Yu, S., Dong, F., Zhang, Q., and Zhou, Y. (2016). Efficient C_3N_4/graphene oxide macroscopic aerogel visible-light photocatalyst. *J. Mater. Chem. A* 4, 7823–7829. doi: 10.1039/C6TA01804A

Wan, W. C., Zhang, R. Y., Ma, M. Z., and Zhou, Y. (2018). Monolithic aerogel photocatalysts: a review. *J. Mater. Chem. A* 6, 754–775. doi: 10.1039/C7TA09227J

Wang, X., Maeda, K., Thomas, A., Takanabe, K., Xin, G., Carlsson, J. M., et al. (2009). A metal-free polymeric photocatalyst for hydrogen production from water under visible light. *Nat. Mater.* 8, 76–80. doi: 10.1038/nmat2317

Wang, X., Liang, Y. H., An, W. J., Hu, J. S., Zhu, Y. F., and Cui, W. Q. (2017). Removal of chromium (VI) by a self-regenerating and metal free g-C_3N_4/graphene hydrogel system via the synergy of adsorption and photo-catalysis under visible light. *Appl. Catal. B Environ.* 219, 53–62. doi: 10.1016/j.apcatb.2017.07.008

Wang, Y. L., Cui, X. B., Yang, Q. Y., Liu, J., Gao, Y., Sun, P., et al. (2016). Preparation of Ag-loaded mesoporous WO_3 and its enhanced NO_2 sensing performance. *Sensors Actuat. B* 225, 544–552. doi: 10.1016/j.snb.2015.11.065

Wei, H. T., Zhang, Q., Zhang, Y. C., Yang, Z. J., Zhu, A. P., and Dionysiou, D. D. (2016). Enhancement of the Cr (VI) adsorption and photocatalytic reduction activity of g-C_3N_4 by hydrothermal treatment in HNO_3 aqueous solution[J]. *Appl. Catal. A General* 521, 9–18. doi: 10.1016/j.apcata.2015.11.005

Yan, S. C., Li, Z. S., and Zou, Z. G. (2009). Photodegradation performance of g-C_3N_4 fabricated by directly heating melamine. *Langmuir* 25, 10397–10401. doi: 10.1021/la900923z

Yang, L. Q., Huang, J. F., Shi, L., Gao, L. Y., Yu, Q., Jie, Y. N., et al. (2017). A surface modification resultant thermally oxidized porous g-C_3N_4 with enhanced photocatalytic hydrogen production. *Appl. Catal. B Environ.* 204, 335–345. doi: 10.1016/j.apcatb.2016.11.047

Yu, J. G., Jin, J., Cheng, B., and Jaroniec, M. (2014). A noble metal-free reduced graphene oxide-CdS nanorod composite for the enhanced visible-light photocatalytic reduction of CO_2 to solar fuel. *J. Mater. Chem. A* 2, 3407–3416. doi: 10.1039/c3ta14493c

Zhang, Q., Zhou, Y., Wang, F., Dong, F., Li, W., Li, H. M., et al. (2014). From semiconductors to semimetals: bismuth as a photocatalyst for NO oxidation in air. *J. Mater. Chem. A* 2, 11065–11072. doi: 10.1039/C4TA01339E

Zhang, R. Y., Wan, W. C., Li, D. W., Dong, F., and Zhou, Y. (2017). Three-dimensional MoS_2/reduced graphene oxide aerogel as a macroscopic visible-light photocatalyst. *Chin. J. Catal.* 38, 313–320. doi: 10.1016/S1872-2067(16)62568-8

Zhang, W. B., Zhai, X. L., Xiang, T. H., Zhou, M., Zang, D. L., Gao, Z. X., et al. (2017). Superhydrophobic melamine sponge with excellent surface selectivity and fire retardancy for oil absorption. *J. Mater. Sci.* 52, 73–85. doi: 10.1007/s10853-016-0235-7

Zhao, J., Guo, Q. J., Wang, X., Xie, H. L., and Chen, Y. Z. (2016). Recycle and reusable melamine sponge coated by graphene for highly efficient oil-absorption. *Colloid Surface A* 488, 93–99. doi: 10.1016/j.colsurfa.2015.09.048

Zhao, S. S., Chen, S., Yu, H. T., and Quan, X. (2012). g-C_3N_4/TiO_2 hybrid photocatalyst with wide absorption wavelength range and effective photogenerated charge separation. *Sep. Purif. Technol.* 99, 50–54. doi: 10.1016/j.seppur.2012.08.024

Zhao, Z., Sun, Y., and Dong, F. (2015). Graphitic carbon nitride based nanocomposites: a review. *Nanoscale* 7, 15–37. doi: 10.1039/C4NR03008G

Zhou, Y., Zhang, X. J., Zhang, Q., Dong, F., Wang, F., and Xiong, Z. (2014). Role of graphene on the band structure and interfacial interaction of Bi_2WO_6/graphene composites with enhanced photocatalytic oxidation of NO. *J. Mater. Chem. A* 2, 16623–16631. doi: 10.1039/C4TA03762F

Zhou, Y., Zhao, Z. Y., Wang, F., Cao, K., Doronkin, D. E., Dong, F., et al. (2016). Facile synthesis of surface N-doped $Bi_2O_2CO_3$: origin of visible light photocatalytic activity and in situ DRIFTS studies. *J. Hazard. Mater.* 307, 163–172. doi: 10.1016/j.jhazmat.2015.12.072